Nano Energy 44 (2018) 174–180

Contents lists available at ScienceDirect

Nano Energy

journal homepage: www.elsevier.com/locate/nanoen

Full paper

3D printed porous carbon anode for enhanced power generation in microbial fuel cell

Bin Bian[a], Dai Shi[a], Xiaobing Cai[a], Mingjun Hu[a], Qiuquan Guo[a], Chuhong Zhang[b], Qi Wang[b], Andy Xueliang Sun[a], Jun Yang[a,*]

[a] Department of Mechanical and Materials Engineering, Western University, London N6A 3K7, Canada
[b] State Key Laboratory of Polymer Materials Engineering (Sichuan University), Polymer Research Institute of Sichuan University, Chengdu 610065, China

ARTICLE INFO

Keywords:
Microbial fuel cell
Shewanella MR-1
3D printing
Porous anode
Carbonization

ABSTRACT

3D porous carbon structures, fabricated via 3D printing technique, were first utilized as the anode materials for microbial fuel cells (MFCs). The intrinsic biocompatibility of 3D printed carbon anodes, together with the open porous structures, greatly enhanced the metabolic activities of microorganisms. The secondary 3D roughness generated from carbon formation functioned as an ideal support for microbial growth, which further increased the surface area of anodes as well. All these factors together determined the exclusive electrochemical performances of MFCs for enhanced power generation and scaling up application. Through carefully tuning the carbonization processes, a multiscale 3D porous carbon structure was achieved for bacterial growth and mass transfer, leading to the highest maximum output voltage, open circuit potential (OCP) and power density for a 300 μm porosity (453.4 ± 6.5 mV, 1256 ± 69.9 mV and 233.5 ± 11.6 mW m^{-2}, respectively). Such performance is superior to that of carbon cloth anode and carbon fiber brush anode under the same condition.

1. Introduction

Microbial fuel cells (MFCs) are devices that use microbes as catalysts to oxidize organic and inorganic matters for electricity generation [1–4] and serve as an ideal technology for wastewater treatment and power output simultaneously [5–7]. Great achievements in electrode materials, operation methods and reactor designs have all contributed to the increase in MFC electricity production [8,9], with extensive studies indicating the significance of the anode materials in improving the performances of MFCs [10,11].

Anode, serving as the bacteria carrier, plays a crucial role on the rate and efficiency of power generation in MFCs. The biocompatibility, efficient transport of nutrient and waste, and surface area are directly affecting the formation of biofilm and proliferation of microbes. Anode materials have been studied for years on properties of corrosion resistance, electrical conductivity, surface area, porosity, and cost [10,12,13]. Niessen et. al. [14] demonstrated anodes consisting of platinum electrocatalyst covered by fluorinated conductive polymer can provide power density of 1350 μA/cm^2. Compared to metal/modified metal anodes, carbon anodes (especially materials with high porosity and large surface area, such as carbon cloth [15], carbon fiber brush [11,16], PPy-CNTs [12], PANI [14], graphene [13,17]) are widely used in MFCs due to their excellent corrosion resistance, good conductivity and biocompatibility. However, pore sizes and structures of MFC anodes, which significantly affect the conductivity, the mass transfer, the amount of bacteria grown on MFC electrodes and thus determine power generation, are not well controlled from existing studies. Porous anodes reported had either too large (> 500 μm) [18,19] or too small (< 10 μm) [20] pores due to the non-controllable manufacturing methods.

Three dimensional printing (3DP), as an effective and unique fabrication technique, allows one to create sophisticated and low-cost devices [21]. Due to its controllability, 3DP has found its applications in various energy research, such as solar cells [22,23], Li-ion batteries [24,25] and skin sensors [26]. Most of 3D printed materials exhibited excellent performances but could reluctantly be used in microbial fuel cells because of cytotoxicity [23], poor conductivity [27] and low porosity [25,26,28,29]. Currently, polymer-based materials are of priority to be used to fabricate 3D objects due to their ease of operation, good biocompatibility and low cost compared to metals and ceramics [30,31]. As mentioned above, the ideal MFC anodes should possess highly porous structures to maximize the bacterial adhesion and power generation, which can be produced precisely using high-resolution 3D printing technology with UV-curable polymer resin. The 3D printed porous polymer structures could be an excellent alternative utilized as MFC anodes as long as we could greatly enhance their electrical

* Corresponding author.
E-mail address: jyang@eng.uwo.ca (J. Yang).

https://doi.org/10.1016/j.nanoen.2017.11.070
Received 12 October 2017; Received in revised form 22 November 2017; Accepted 30 November 2017
Available online 06 December 2017
2211-2855/ © 2017 Elsevier Ltd. All rights reserved.

conductivity. Thus, an effective modification must be implemented.

Usually, metals [17,32] and carbon based materials can be used as MFC anode materials. Zhu. X and B.E. Logan [32] compared copper, stainless steel and carbon cloth as MFC anodes, and concluded that carbon-based anodes had superior performances on power generation owing to its high specific surface area and good biocompatibility. To produce porous carbonaceous electrodes from 3D printed polymer structures, carbonization processes could be proposed and optimized, so that the good biocompatibility could be achieved for the carbonized materials with basic 3D porous architectures preserved [33].

In this study, 3D printed carbonaceous porous (3D-PCP) anode structures were fabricated via polymer 3D printing technique followed by a controlled carbonization process, leading to anode materials with good conductivity and excellent biocompatibility [33,34]. Besides, the precisely controlled morphology and pore sizes were mapped into the carbonized anodes, which were proportionally scaled down from the printed structures to achieve a controlled 3D porous carbon structure. The intrinsically generated secondary porous surface during carbonization of the 3DP polymer further increased the contact area for microbe adhesion. With the hieratically porous structure, both the metabolic activities and proliferation of microbes were greatly enhanced, leading to superior performances of MFC power generation.

2. Experiment

2.1. Fabrication of 3D printed anode

The porous anode structures were designed by Solidworks and printed out in a layer-by-layer manner by a DLP (digital light processing) 3D printer (Asiga) with UV curable resin (Clear 2005T resin from Miicraft). The burn-in exposure and normal exposure time for the 3D printer were 5 s and 0.5 s, respectively; while the layer thickness was set as 25 μm. The 3D printed structures were treated by sonication in ethanol for 10 min and washed 3 times by DI water to remove any uncured polymer. The structures were dried in air before use.

Carbonization process of the 3D printed structures was conducted in a tube furnace (Lindberg/Blue M, Thermo Scientific), which was continuously purged with pure N_2 at a flow rate of 3 L/min to avoid anode oxidation and collapse. The heating temperature gradually rise from room temperature to 800 °C and then cooled down to room temperature. As a shrinkage ratio of 2.3:1 during carbonization was found in pre-tests for all 3D printed materials, different 3D porous structures were designed, with the same 6.325 cm-diameter, 1.15 cm-thickness and five different pore sizes of 230 μm, 460 μm, 690 μm, 920 μm and 1150 μm, to obtain anode architectures with 2.75 cm-diameter, 0.5 cm-thickness and pore sizes ranging from 100 μm to 500 μm after carbonization. SEM were carried out after 3D-PCP anode preparation.

2.2. MFC construction and operation

Single-chamber MFCs (Phychemi, 4 cm long, 3 cm inner diameter, 28 ml volume) with an air cathode (carbon cloth coated with 0.5 mg/cm^2 Pt/C, Fuel Cells Etc) were constructed with the carbonized 3D anodes prepared above, as shown in Fig. 1. The space between each anode and cathode was 2 cm and the MFC chambers were sealed with epoxy and dried before use. The cell voltage across a 1000 Ω external resistor in the circuit was monitored every 5 min using a high–-resolution DAQ device (NI USB 6251 BNC) and the LabVIEW software package (National Instruments).

Shewanella oneidensis MR-1 (wild-type) was cultured aerobically in Tryptic Soy Broth (TSB, BD) for 3 days in a 30 °C water bath with shaking at 150 rpm. Biocompatibility of the 3D-PCP anode materials was tested with the same bacterial strains in comparison with the carbon cloth anode (see Supplementary information). Bacteria were then centrifuged (5000 rpm, 6 min) and washed three times in PBS buffer (Dulbecco's, Sigma) before adjusting to the desired concentration. The washed cells were inoculated into MFCs with the growth medium (containing 18 mM lactate) used by Bretschger et al. [35]. Vitamins and mineral solution (ATCC) were added after filtration (0.2 μm filters, VWR).

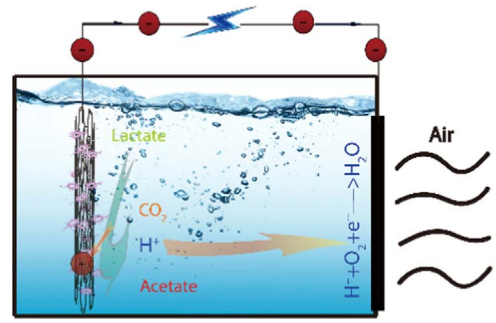

Fig. 1. Schematic of an air-cathode MFC configuration.

MFCs were first inoculated with 50% inoculum of S. oneidensis MR-1 and 50% medium. The medium in MFCs was replaced every 2.5 days until all MFCs produced relatively stable voltages. All the MFC experiments were conducted in duplicates and in batch mode at room temperature.

2.3. MFC characterization

MFC polarization curves were measured in linear sweep voltammetry (LSV) with a potentiostat (CHI 1200a, CH Instruments Inc.), at a scanning rate of 0.1 mV s^{-1} from open circuit potential (OCP) to 0.01 mV. Power densities were calculated based on the polarization curves and the cathode projected surface area (6 cm^2). Multi-potentiostat (VMP3, BioLogic) was used for Electrochemical Impedance Spectroscopy (EIS) measurement in a two-electrode mode with frequency ranging from 100 kHz to 10 mHz. An AC signal amplitude of 5 mV was chosen. The anode served as the working electrode and the cathode was used as the counter and reference electrode. MR-1 cells on the anodes after over 40 days' MFC running were fixed in 3% glutaraldehyde solution at 4 °C overnight and rinsed in DI water. The anodes were then dehydrated through a graduated series of ethanol (20%, 40%, 60%, 80%, 100%, 100%, and 100%) and air dried before biofilm characterization by SEM (S-4500, Hitachi) with gold deposition.

3. Results and discussion

3.1. Carbonization and surface morphology of 3D-PCP anodes

To find out the properties of 3D porous structures and better control the carbonization processes, thermogravimetric analysis (TGA) was conducted to analyze the decomposition pattern of the cured resin and determine the carbon yields.

In Fig. 2a, the mass percentage of Miicraft resin was measured as a function of temperature. From 25 °C to 350 °C, no significant mass

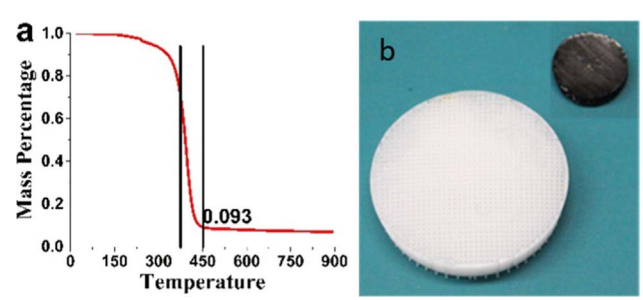

Fig. 2. (a) TGA analysis of the Miicraft resin as a function of temperature; (b) the size comparison of 3D printed porous structures before and after carbonation.

change occurred (~ 80 wt% remaining at 350 °C). However, a sharp drop was observed from 350 °C to 450 °C, with a carbon yield of 9.3 wt % at 450 °C and 7.3 wt% at 800 °C. Based on the TGA results, 3D printed porous structures were carbonized through three heating phases to optimize the carbonization processes. Phase 1 was 25 °C–350 °C and the heating rate was set at 3 °C/min; phase 2 was 350 °C–450 °C with the heating rate of 0.2–1.5 °C/min to minimize the structure collapse due to the high rate of decomposition; and phase 3 was 450 °C–800 °C with a heating rate of 2 °C/min.

During the carbonization processes, the carbonized structure needs to be strong enough to maintain the lattice architecture. Thus, the stage with major mass loss, i.e. Phase 2, was tuned to optimize the integrity and mechanical properties of the carbonaceous anode. Before Phase 2, 45 min holding time was applied at 350 °C to evaporate the volatile and uncross-linked compounds in the UV-cured 3D structures (See Table S1 in SI). The heating rate at phase 2 was adjusted to 0.4 °C/min to successfully minimize the structure collapse during carbonization. 3D-PCP anodes with graphitic structures, excellent conductivity and a shrinkage ratio of 2.3:1 were obtained after 2 h heat treatment at 800 °C as shown in Fig. 2b.

Through 3D printing and precise control of carbonation processes, the desired open porous carbonaceous anodes with free standing characteristics were fabricated. SEM images in Fig. 3a–e illustrated the dimensions of all the five 3D-PCP anode structures. After careful calculation and adjustment, 3D porous structures were precisely printed and carbonized. The error level of anode pore size was less than ± 3.5% (except the 100 μm porous one which had an error level of about 15% due to the higher internal stress during carbonization processes), which exhibited great advantages of utilizing 3D printing technology for repeatable porous electrode fabrication.

Besides, these highly porous architectures provided more surface area (both inner and outer) for bacterial growth, achieving a total porosity of over 95%. Apart from the 100–500 μm macro porous structures, the surface morphology, as shown in Fig. 3g–j, indicated that secondary porous surface structures were formed after carbonization and uniformly distributed on the surface of 3D-PCP anodes with high density. The secondary porous valleys from 2 to 5 μm located at the carbon matrix were very suitable for bacterial adhesion and growth, which efficiently increased the specific surface area of 3D-PCP anodes and would definitely further enhance the MR-1 biofilm formation and increase bacterial cell densities. Higher resolution SEM images of the 3D-PCP anode surface of Fig. 3g were presented in Fig. S1, demonstrating there were no nano-valleys formed even though the surface was pretty rough. According to Lorenzetti et al., macroscopic porous structures usually provided a preferential site for bacteria adhesion on the electrode surface, while the actual microbe-electrode interaction was determined by the microscopic roughness of the valleys (> 1 μm) rather than the nano-roughness of the materials [36].

It was also believed that the microscopic valleys would lead to an "interlocking" effect and higher bacterial adhesion on the substrate. As bacterial densities on the anodes play a crucial role in electricity output, 3D-PCP anodes were expected to produce higher power densities. In addition, for the long term sustainable application, the open porous structure was ideal for the transport of nutrient and waste. As the size of MR-1 cells was far less than major pore sizes of these 3D-PCP anode structures, MR-1 cells were allowed to migrate inside-out easily, which leads to sufficient mass transfer and enhanced metabolic activities. When we looked at the surface of carbon cloth, elastic carbon fibers were found intersecting each other, shown in Fig. 3f, and formed blank space with a total porosity of 80%. However, the surface of fibers were glossy with no secondary pores distributed, which provided less space for bacterial colonization compared with 3D-PCP anodes. EDX analysis was also conducted for 3D-PCP anodes and 4.7 wt% nitrogen element was found after carbonization, which is illustrated in Fig. 3l. As N-doped carbon materials were believed to have better electron transfer efficiency [37], electro-catalytic property [38] and excellent

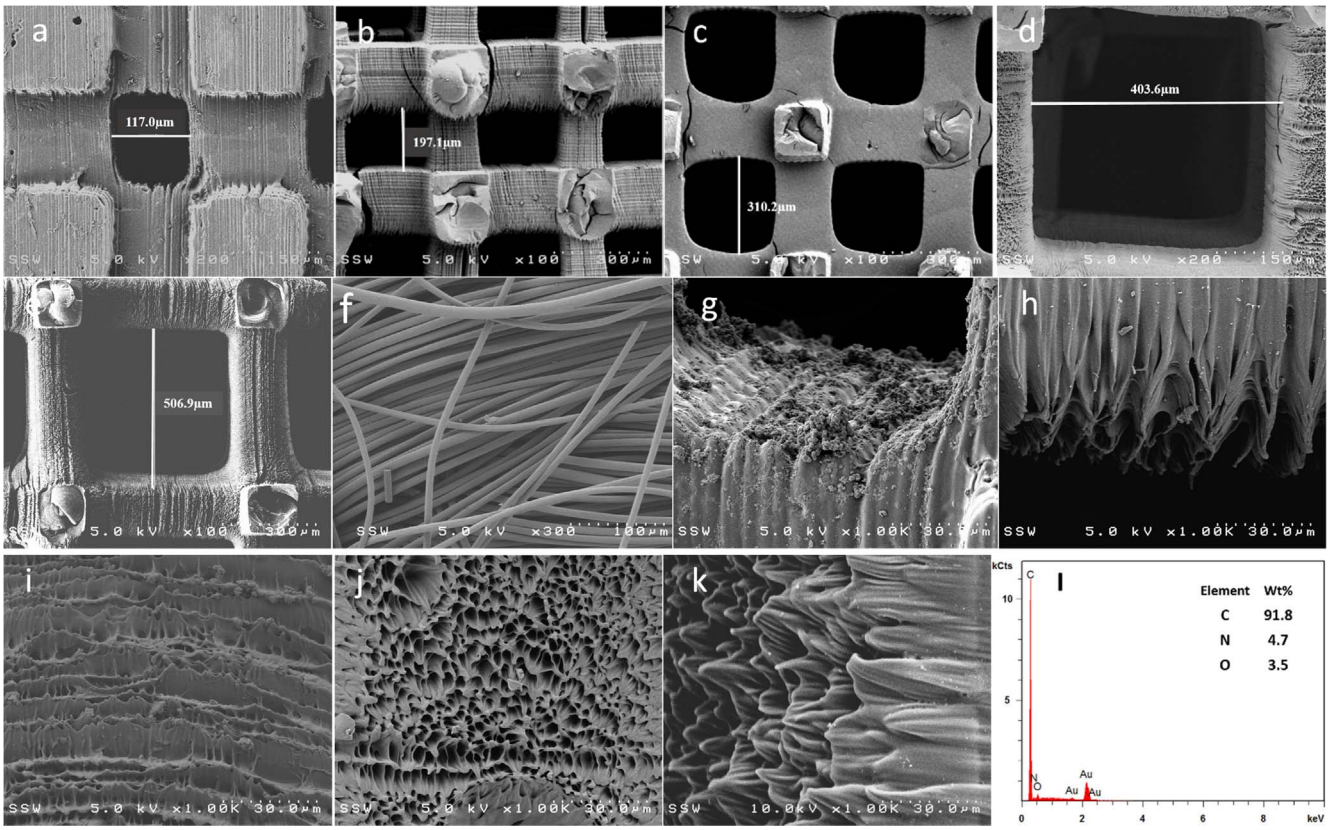

Fig. 3. (a) – (e) are SEM images of well printed 3D-PCP anodes with pore sizes from 100 μm to 500 μm. (g) – (k) show the rough structures on 3D porous anode surface. (f) is carbon cloth surface and (l) presents EDX data of carbonized anode.

biocompatibility [39,40], the 3D-PCP anodes were expected to be more suitable for bacterial growth in MFCs. As to the cost, less than $2 was spent on each 3D-PCP anode fabrication, which was far less than the other kind of commonly used 3D anode ($0.05 carbon fiber, $5.64 titanium wire), carbon fiber brush. SI Table S2 shows the cost of the 3D-PCP anodes compared with the carbon fiber brush anode commonly used in MFC research [10,16]. This comparison is based on the same project surface area and the cost of materials from suppliers. Although the carbon fibers cost very little, the titanium wires used to bind the carbon fibers are over 3 times more expensive than the 3D-PCP anodes. Importantly, the cost of UV-curable resins could be further reduced after optimization.

3.2. Maximum voltage measurement

The biocompatibility of the 3D-PCP anodes were examined by a standard method (See description in SI for more details) [41,42]. The biofilm formation on the 3D-PCP anode surface was much more condense compared with that on carbon cloth, which was visually confirmed in Fig. S2 and demonstrated the good surface biocompatibility and excellent bacterial adhesion on 3D-PCP electrodes. This result is consistent with the previous studies on the application of carbonaceous electrodes in MFCs showing excellent electricity generation performance [43,44].

MFCs with 3D-PCP anodes were operated for more than 40 days until stable voltages were monitored in several consecutive cycles. After stabilization, the voltage generated by each MFC maintained a constant maximum value and dropped at the end of each cycle. Data from Fig. 4 illustrated that the 300 μm porous carbon anode produced the largest maximum voltage of 453.4 ± 6.5 mV while only 188.5 ± 2.7 mV was achieved by the MFC with carbon cloth anode. To better understand the performances of MFCs with 3D printed anodes, the maximum voltages of each MFCs were recorded and it was found that all 3D-PCP anodes produced much higher maximum voltages than that of the carbon cloth anode, with an increase by 33.7–138.4% depending on the anode pore sizes. 3D-PCP anodes with 200 μm and 300 μm pores achieved > 2 times higher maximum voltages than the carbon cloth anode (410.2 ± 6.3 mV, 453.4 ± 6.5 mV and 188.5 ± 2.7 mV, respectively), which exhibited great advantages of 3D-PCP anodes over the plain carbon cloth anode. As we mentioned above that the surface area and porosity of 3D-PCP anodes were much higher than carbon cloth electrode (95% > 80%), far more bacterial cells were believed to grow on the 3D structures than carbon cloth. The higher density of bacteria was one of the most important factors for enhanced electricity production. Besides, 3D porous carbon anodes are more efficient for interfacial charge transfer [45] and more biocompatible [46], so a reduced overpotential could be obtained for oxidation of organic matters by bacterial cells. All of these would contribute to the higher maximum voltages by 3D porous carbon anodes.

3.3. OCP and power density

OCPs and power densities were collected using LSV for all the six MFCs and results showed that all MFCs with 3D-PCP anodes obtained higher OCPs than carbon cloth anode, except the MFC with the 100 μm 3D-PCP anode. OCPs of 651.45 ± 18.03 mV, 1194.5 ± 16.23 mV, 1256.0 ± 9.90 mV, 888.5 ± 30.26 mV and 749.95 ± 16.19 mV were achieved for 100–500 μm 3D-PCP anodes, respectively, in comparison to 669.35 ± 5.16 mV from carbon cloth anode. Valerie Watson et al. [45] utilized the 3D carbon fiber brush as the anode in MFC operation and eventually obtained an OCP of 800 mV, which was also far less than those from 3D-PCP printed carbon anodes with pore sizes ranging from 200 μm to 400 μm. Since the electricity generation in MFCs is positively correlated with bacterial cell density and microbe-electrode interaction, more biofilm and electroactive sites (due to nitrogen-doping) on the surface of secondary pores may account for the supreme voltage generation from MFCs equipped with 3D-PCP anodes.

Besides, 3D-PCP anodes generated exclusive power densities compared to the carbon cloth anode. Polarization curves plotting voltage as a function of current were measured when the maximum voltages produced by all MFCs were constant over cycles, to evaluate the influences of porous structures on anodic electrochemical behaviors of MR-1 fed by lactate. The maximum

power density generated by the MFC with carbon cloth anode reached 69.0 ± 4.7 mW m^{-2}, compared to 233.5 ± 11.6 mW m^{-2} attained by the 300 μm 3D-PCP anode. It was clearly shown in Fig. 5 that the 3D-PCP anodes greatly enhanced the capability of power generation in MFCs and increased the power density by 22–238.4%, indicating the excellent electrochemical properties of 3D-PCP anodes. Maximum power densities from the Shewanella MR-1 culture decreased in the order: 300 μm > 200 μm > 400 μm > 100 μm > 500 μm > carbon cloth (Table 1), which followed the same trend in maximum voltage generation, except that the maximum voltage produced by the 100 μm 3D-PCP anode (281.9 ± 12.7 mV) was higher compared to the 500 μm one (241.3 ± 26.4 mV). The finding of the highest power density and voltage from 300 μm 3D-PCP anode was unexpected as the specific surface area of this electrode was much lower compared with the 100 μm one, which should have had more bacterial adhesion and better electrochemical performances. We also compared our results to the

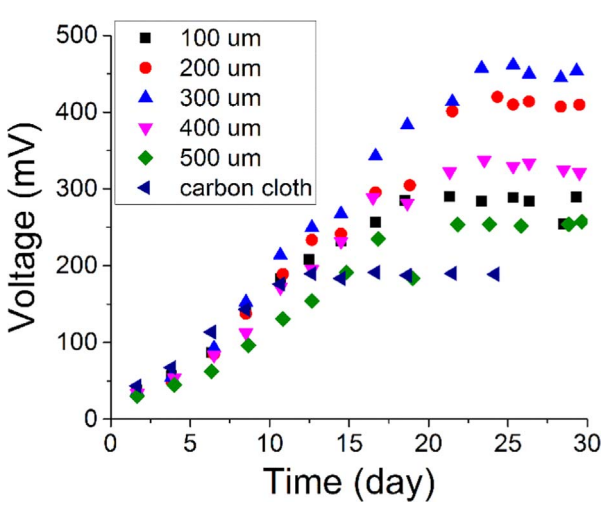

Fig. 4. Voltage generation of MFCs with 3D-PCP anodes with pore sizes of 100–500 μm and with a carbon cloth anode.

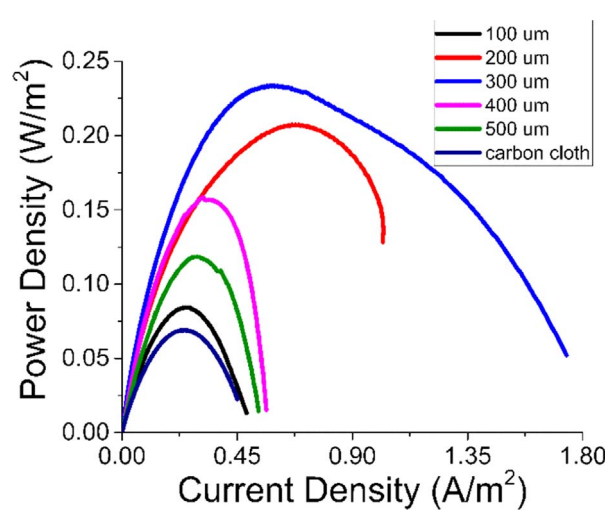

Fig. 5. The power density curves of MFCs with 3D-PCP anodes with pore sizes of 100–500 μm, based on the same projected surface area of the air-cathode (6 cm^2).

Table 1
Fitting results of the solution resistance and the charge transfer resistance of each MFC anode and power density for each MFC configuration.

Anode Structure	Pore Size/μm	R_S/ Ω	R_{ct}/Ω	Max voltage/mV	OCP/mV	Max power density/ mW m^{-2}
3D -PCP anode	100	25.0	22.4	281.9 ± 12.7	651.5 ± 18.0	80.9 ± 3.3
	200	23.3	19.4	410.2 ± 6.3	1194.5 ± 16.2	198.4 ± 8.9
	300	22.8	23.9	453.4 ± 6.5	1256.0 ± 9.9	233.5 ± 11.6
	400	30.3	16.4	328.1 ± 6.5	888.5 ± 30.3	154.6 ± 3.6
	500	19.6	23.2	241.3 ± 26.4	750.0 ± 16.2	103.1 ± 15.3
Carbon cloth anode	N/A	32.8	13.5	188.5 ± 2.7	669.4 ± 5.2	69.0 ± 4.7

power output (148 ± 20 mWm^{-2}) by the carbon fiber brush anode [45], it was discovered that comparable performances could be obtained, with 200 μm and 300 μm 3D-PCP anodes producing higher power densities, while 100 μm and 500 μm 3D-PCP anodes generated slightly lower power output (80.9 ± 3.3 mW m^{-2} and 103.1 ± 15.3 mW m^{-2}, respectively). All above shows that 3D printing technology could contribute to higher performances of MFCs after optimization.

Coulombic efficiency (CE) was obtained utilizing the ratio of the total coulombs produced ($C = \sum_{t=1}^{T} (E \times t)/R$) during the experiment to the theoretical amount of coulombs available ($C_t = 4FCV$, F: Faraday's constant, C: lactate concentration, V: reactor volume) from the oxidation of lactate to acetate [47]. CEs of the MFCs with different anode configurations ranged between 8.5% and 15.5% (Fig. 6). Among all the six reactors, MFC with 300 μm 3D-PCP anode achieved the highest CE of 15.34 ± 0.062%, which was 75.5% higher than MFC with carbon cloth anode (8.74 ± 0.137%). All MFCs equipped with 3D-PCP anodes exhibited relatively high CE (> 10%), indicating the high efficiency of electron and mass transfer. As reported by Tang et al. [47], electrical current could only be produced when lactate is oxidized to acetate with 4 mol e^-/mol lactate in anaerobic conditions. This results in the lower CE compared with other MFCs inoculated with mixed culture [16].

3.4. Electrochemical impedance spectroscopy

EIS is powerful technique and usually employed to analyze electrochemical systems. The internal resistance of the MFCs can be interpreted from the semicircle shape of Nyquist plots in EIS of the six anode architectures. The equivalent circuit of EIS fitting for all anode analysis was shown in Fig. 7g. R_s is the solution resistance and R_{ct} is relevant to the charge transfer resistance. The fitting was conducted utilizing Zview software. From Fig. 7a-f, it could be seen that EIS data was well fitted. The diameters of the semicircles correspond to the charge transfer resistance and the values of the first intersections in each plot with X-axis represent the solution resistances. The results of the solution resistance

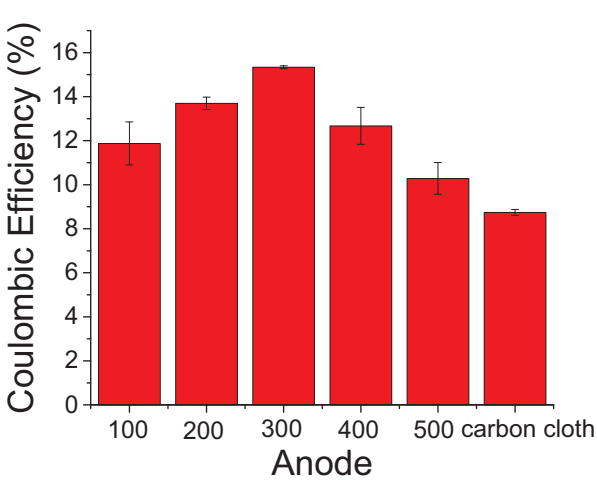

Fig. 6. Coulombic efficiencies for Shewanella oneidensis MR-1 (lactate to acetate) in MFCs with 3D-PCP and carbon cloth anodes.

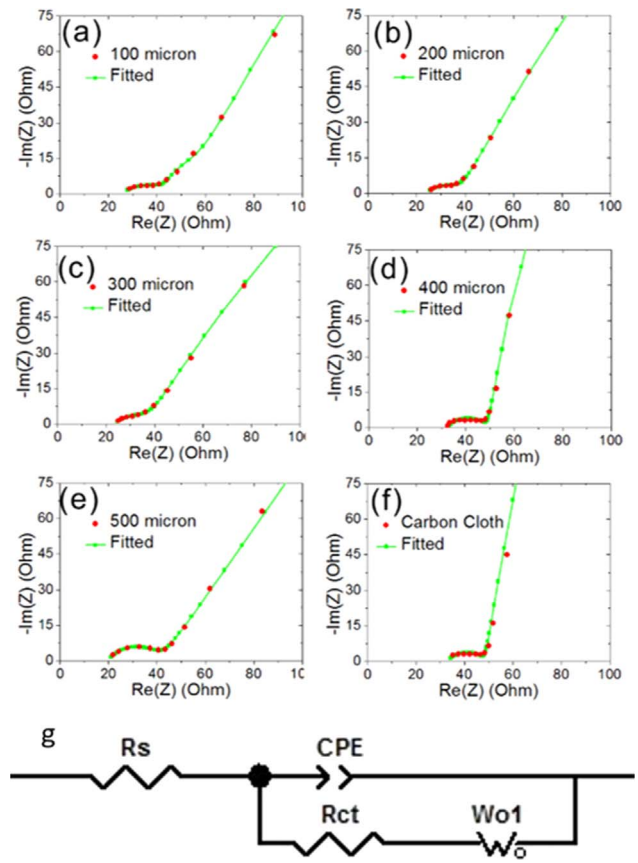

Fig. 7. (a)-(f) Nyquist plots of EIS data for different anode structures (red line), and equivalent circuit model fit (green line). Note that the circle fit provides excellent agreement with the data. (g) is the equivalent circuit model used to fit MFC anode response to EIS experiments.

and the charge transfer resistance of each MFC were listed in Table 1.

From Table 1, the average solution resistance of MFCs with 3D-PCP anodes was 24.2 Ω, which was about 8.6 Ω lower compared to the MFC with carbon cloth anode, while the charge transfer resistance of the carbon cloth anode was a little bit lower than that of 3D-PCP anodes. The lower solution resistances of 3D-PCP anodes demonstrated better mass transfer between solution and 3D-PCP anodes, which indicated that more nutrients were accessible for bacterial growth. Among all the five 3D-PCP anodes, the one with 500 μm pores obtained the lowest solution resistance, since it has the biggest open porous structure. Merkey et al. [48] simulated biofilm growth on the MFC anode and found that nutrient transfer to the biofilm surface was the primary driver of the energy production in MFCs. From Table 1, we could clearly witness a trend of electricity generation enhancement with the increase of pore sizes from 100 to 300 μm, which is mainly attributed to the improved nutrient transfer capability of 3D-PCP anodes. However, the current production is also related to biofilm formation on the anode, which lead to abnormal decrease of power outputs from 3D-PCP anodes with pore sizes from 300 to 500 μm and the low performance of the

carbon cloth anode. The total resistance ($R_s + R_{ct}$) of 3D-PCP anodes was almost the same with that of carbon cloth anode. The solution resistance and the charge transfer resistance measured were also comparable to the amount measured using graphite fiber brush anode by Bin Wei et. al. [49] (~ 45 Ω), which indicated the excellent electrochemical properties of 3D-PCP anodes. As the smaller slopes of the curves at low frequency indicate the higher roughness of electrode materials, 3D-PCP anodes were demonstrated to have more sophisticated surface morphology, and thus provide more surface area for bacterial adhesion, compared to the carbon cloth electrode, which agrees well with the SEM images in Fig. 3.

3.5. SEM images of 3D printed carbonized anode and carbon cloth

In order to investigate the impacts of 3D porous morphology on bacterial growth on MFC anodes, FESEM was carried out to observe the biofilm formation on the six MFC anodes after 40 days of MFC operation. It was found that the outer surface of both 3D-PCP structures and the carbon cloth anode was fully covered by thick layers of bacterial biofilm and extracellular polymeric substances (EPS) (Fig. 8f, g). Bacteria produce EPS to prompt cell attachment on anode surface, aggregation, and biofilm formation. The length of the MR-1 cells was several microns and EPS were generated to connect the bacterial cells. All above ensures that the electrons produced in the organic oxidation reaction could be transferred onto the carbon anode surface. Apart from the biofilm on the outer surface, MR-1 cell aggregation was also discovered on the inner surface of 3D-PCP anodes. Lots of MR-1 colonization and EPS were found growing and connecting with each other across the internal pores of 3D-PCP anodes, which agreed well with the previous reports that macroporous structures with pore sizes ranging from tens to hundreds microns had more bacterial adhesion and better mass transfer, compared to 2D plain electrode materials [13,17]. This could lead to higher electricity output for 3D-PCP anodes comparing to the carbon cloth anode. As mentioned, microorganisms grown on the outer porous layer had easier access to platonic cells and nutrients, there were slightly more bacteria adhering to outer porous layers than inner ones.

Another interesting observation was that the density of the bacterial biofilm was heavily dependent on the different pore sizes of the 3D anodes (Fig. 8a–e). The inner surface of the 300 μm pore-sized anode was observed to have the best and highest bacterial density accumulated, while the 100 μm porous anode had the lowest. This explains the best performance achieved, such as maximum cell voltage, power density and CE, from MFCs with the 300 μm 3D-PCP anode. As shown in Table 1, the solution resistances of 100 μm and 200 μm anode structures were 2.2 and 0.5 Ω higher than the 300 μm anode, respectively, which indicated poorer mass transfer from the medium into the internal area and resulted in the low cell density on the inner surface of 100 μm and 200 μm 3D-PCP anodes. This is commonly seen when dense biofilm grow extensively to merge the anode flow channels (Fig. 8f) and limit nutrient influent to interior regions [48,50]. Another potential drawback of the limited mass transfer is the corresponding loss of inner surface area of 3D-PCP anodes because of the low coverage of MR-1 biofilm (Fig. 8a-b). 100 μm 3D-PCP anode has the largest surface area among all the five 3D-PCP anodes with the same 3D dimensions and volume. However, due to the bio-clogging and smaller open porous structures, the inner surface area was not fully used by MR-1 cells, which indicates the potential shortage of micro or mesoporous electrode materials in

MFCs [48,51]. Bacterial biofilm on the inner surface of 400 μm and 500 μm 3D-PCP anodes were uniform but visually as thick as the one formed on the 300 μm porous anode. However, large loopholes were observed in the biofilm on these two anodes, whose sizes increased with the pore sizes of the anodes. This indicates the increasing difficulty to form strong connections between EPS and bacterial cells with the increase of pore size. As the power output of MFCs mainly depends on the amount of electrons and the electron transfer between anodes and bacterial biofilm, the loopholes in the biofilm might result in the slightly inferior electrochemical performance of MFCs with these two anodes. Thus, the MFC with around 300 μm 3D-PCP anode was demonstrated to have the best electrochemical performances.

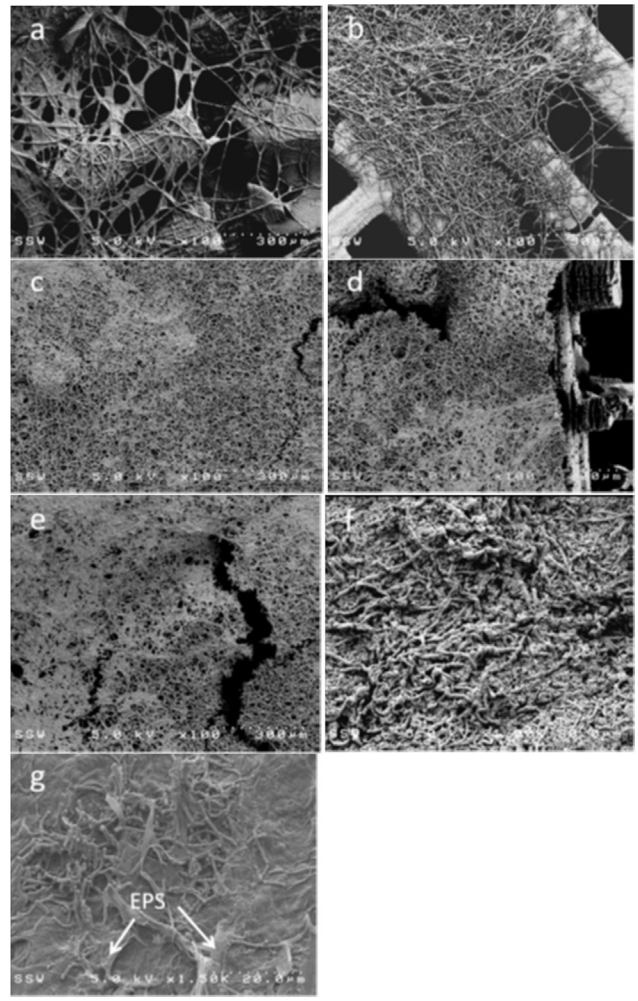

Fig. 8. FESEM images of Shewanella MR-1 biofilm formed on the internal pore surfaces of 3D-PCP anodes ((a):100 μm, (b):200 μm, (c):300 μm, (d):400 μm, (e):500 μm), (f), (g) showed the biofilm formation on the outer surface of 3D-PCP anode and carbon cloth anode, respectively. Besides, extracellular polymeric substances (EPS) were observed in the sample.

4. Conclusion

In this study, 3D porous carbon anodes were precisely fabricated by 3D printing technique and a controlled carbonization process, which was applied for the first time to air-cathode MFCs. Compared to the 2D plain anode materials, 3D anode shows significantly improved electrochemical performances, which were attributed to their larger surface area, better mass transfer, excellent biocompatibility and enhanced bacterial adhesion. The 300 μm 3D-PCP anode was proven to obtain the best electrochemical properties, in terms of maximum voltages, OCPs, power densities and CEs, among all other 3D-PCP anodes, which demonstrated the necessary of electrode pore tuning in MFCs and denied the common belief of strong correlation between higher surface area and better MFC performances. With 3D printing technology, the pore sizes of the 3D-PCP anodes could be tuned to achieve an optimized balance between surface area, mass transfer and metabolic activities for the best MFC performances. Overall, the hybrid of 3D printing and carbonization approach is a promising technique for us to study MFC

systems at low costs and has great potential to scale up MFC reactors for waste stream treatment in the future.

Acknowledgements

The author is grateful for the financial support from the Natural Science and Engineering Research Council of Canada (NSERC) STPGP 447623, UAC award from Xerox, and Research Accelerator Grant Program of the University of Western Ontario.

Appendix A. Supplementary material

Supplementary data associated with this article can be found in the online version at http://dx.doi.org/10.1016/j.nanoen.2017.11.070.

References

[1] R.S. Berk, J.H. Canfield, Appl. Microbiol. 12 (1964) 10.
[2] J.R. Rao, G.J. Richter, F. Vonsturm, E. Weidlich, Bioelectrochem. Bioenerg. 3 (1976) 139–150.
[3] J.B. Davis, H.F. Yarbrough, Science 137 (1962) 615.
[4] M.C. Potter, Proc. R. Soc. Lond. B-Conta 84 (1911) 260–276.
[5] B.E. Logan, Microbial Fuel Cells, John Wiley & Sons, USA, 2008.
[6] V. Gadhamshetty, N. Koratkar, Nano Energy 1 (2012) 3–5.
[7] H.Y. Wang, F. Qian, Y. Li, Nano Energy 8 (2014) 264–273.
[8] P. Liang, J.C. Wei, M. Li, X. Huang, Front. Environ. Sci. Eng. 7 (2013) 913–919.
[9] B.E. Logan, M.J. Wallack, K.Y. Kim, W.H. He, Y.J. Feng, P.E. Saikaly, Environ. Sci. Technol. Let. 2 (2015) 206–214.
[10] V. Lanas, Y. Ahn, B.E. Logan, J. Power Sources 247 (2014) 228–234.
[11] J.C. Wei, P. Liang, X. Huang, Bioresour. Technol. 102 (2011) 9335–9344.
[12] Y.J. Zou, C.L. Xiang, L.N. Yang, L.X. Sun, F. Xu, Z. Cao, Int. J. Hydrog. Energy 33 (2008) 4856–4862.
[13] H.Y. Wang, G.M. Wang, Y.C. Ling, F. Qian, Y. Song, X.H. Lu, S.W. Chen, Y.X. Tong, Y. Li, Nanoscale 5 (2013) 10283–10290.
[14] J. Niessen, U. Schroder, M. Rosenbaum, F. Scholz, Electrochem. Commun. 6 (2004) 571–575.
[15] Y. Yuan, S.G. Zhou, L. Zhuang, J. Power Sources 195 (2010) 3490–3493.
[16] B. Logan, S. Cheng, V. Watson, G. Estadt, Environ. Sci. Technol. 41 (2007) 3341–3346.
[17] X. Xie, G.H. Yu, N. Liu, Z.N. Bao, C.S. Criddle, Y. Cui, Energy Environ. Sci. 5 (2012) 6862–6866.
[18] X. Xie, L.B. Hu, M. Pasta, G.F. Wells, D.S. Kong, C.S. Criddle, Y. Cui, Nano Lett. 11 (2011) 291–296.
[19] Y.C. Yong, X.C. Dong, M.B. Chan-Park, H. Song, P. Chen, ACS Nano 6 (2012) 2394–2400.
[20] Z.M. He, J. Liu, Y. Qiao, C.M. Li, T.T.Y. Tan, Nano Lett. 12 (2012) 4738–4741.
[21] M. Geissler, Y.N. Xia, Adv. Mater. 16 (2004) 1249–1269.
[22] D. Vak, K. Hwang, A. Faulks, Y.S. Jung, N. Clark, D.Y. Kim, G.J. Wilson, S.E. Watkins, Adv. Energy Mater. 5 (2015).
[23] D. Angmo, T.T. Larsen-Olsen, M. Jorgensen, R.R. Sondergaard, F.C. Krebs, Adv. Energy Mater. 3 (2013) 172–175.
[24] K. Sun, T.S. Wei, B.Y. Ahn, J.Y. Seo, S.J. Dillon, J.A. Lewis, Adv. Mater. 25 (2013) 4539–4543.
[25] A. Izumi, M. Sanada, K. Furuichi, K. Teraki, T. Matsuda, K. Hiramatsu, H. Munakata, K. Kanamura, J. Power Sources 256 (2014) 244–249.
[26] P. Salvo, R. Raedt, E. Carrette, D. Schaubroeck, J. Vanfleteren, L. Cardon, Sens. Actuators a-Phys. 174 (2012) 96–102.
[27] X.J. Wei, D. Li, W. Jiang, Z.M. Gu, X.J. Wang, Z.X. Zhang, Z.Z. Sun, Sci. Rep.-Uk 5 (2015).
[28] A. Chiappone, I. Roppolo, E. Naretto, E. Fantino, F. Calignano, M. Sangermano, F. Pirri, Compos. Part B-Eng. 124 (2017) 9–15.
[29] D. Zhang, B.H. Chi, B.W. Li, Z.W. Gao, Y. Du, J.B. Guo, J. Wei, Synth. Met. 217 (2016) 79–86.
[30] S. Bose, S. Vahabzadeh, A. Bandyopadhyay, Mater. Today 16 (2013) 496–504.
[31] B.C. Gross, J.L. Erkal, S.Y. Lockwood, C.P. Chen, D.M. Spence, Anal. Chem. 86 (2014) 3240–3253.
[32] X.P. Zhu, B.E. Logan, J. Chem. Technol. Biotechnol. 89 (2014) 471–474.
[33] S. Ryu, C. Lee, J. Park, J.S. Lee, S. Kang, Y.D. Seo, J. Jang, B.S. Kim, Angew. Chem. Int. Ed. 53 (2014) 9213–9217.
[34] F. Zhang, M. Wei, V.V. Viswanathan, B. Swart, Y. Shao, G. Wu, C. Zhou, Nano Energy 40 (2017) 418–431.
[35] R. Ray, S. Lizewski, L.A. Fitzgerald, B. Little, B.R. Ringeisen, J. Microbiol. Methods 82 (2010) 187–191.
[36] M. Lorenzetti, I. Dogsa, T. Stosicki, D. Stopar, M. Kalin, S. Kobe, S. Novak, ACS Appl. Mater. Interfaces 7 (2015) 1644–1651.
[37] Y. Wang, Y.Y. Shao, D.W. Matson, J.H. Li, Y.H. Lin, ACS Nano 4 (2010) 1790–1798.
[38] L. Jia, D.H. Wang, Y.X. Huang, A.W. Xu, H.Q. Yu, J. Phys. Chem. C 115 (2011) 11466–11473.
[39] W.P. Wang, Y.C. Lu, H. Huang, J.J. Feng, J.R. Chen, A.J. Wang, Analyst 139 (2014) 1692–1696.
[40] A. Barati, M. Shamsipur, E. Arkan, L. Hosseinzadeh, H. Abdollahi, Mater. Sci. Eng. C-Mater. 47 (2015) 325–332.
[41] S.J. Park, Y.S. Jang, J. Colloid Interface Sci. 261 (2003) 238–243.
[42] M.A. Correa-Duarte, N. Wagner, J. Rojas-Chapana, C. Morsczeck, M. Thie, M. Giersig, Nano Lett. 4 (2004) 2233–2236.
[43] H.L. Zhu, H.M. Wang, Y.Y. Li, W.Z. Bao, Z.Q. Fang, C. Preston, O. Vaaland, Z.Y. Ren, L.B. Hu, Nano Energy 10 (2014) 268–276.
[44] J. Liu, Y. Qiao, C.X. Guo, S. Lim, H. Song, C.M. Li, Bioresour. Technol. 114 (2012) 275–280.
[45] V.J. Watson, B.E. Logan, Biotechnol. Bioeng. 105 (2010) 489–498.
[46] T.H. Han, S.Y. Sawant, S.J. Hwang, M.H. Cho, RSC Adv. 6 (2016) 25799–25807.
[47] Y.J.J. Tang, A.L. Meadows, J.D. Keasling, Biotechnol. Bioeng. 96 (2007) 125–133.
[48] B.V. Merkey, D.L. Chopp, Bull. Math. Biol. 74 (2012) 834–857.
[49] B. Wei, J.C. Tokash, F. Zhang, Y. Kim, B.E. Logan, Electrochim. Acta 89 (2013) 45–51.
[50] G. Feng, Y. Cheng, S.-Y. Wang, D.A. Borca-Tasciuc, R.W. Worobo, C.I. Moraru, Npj Biofilms Microbiomes 1 (2015) 15022.
[51] T.R.R. Pintelon, C. Picioreanu, M.C.M. van Loosdrecht, M.L. Johns, Biotechnol. Bioeng. 109 (2012) 1031–1042.